Oscillation of cylinders of rectangular cross section immersed in fluid

Douglas R. Brumley, Michelle Willcox, and John E. Sader[a)]
Department of Mathematics and Statistics, The University of Melbourne, Victoria 3010, Australia

(Received 11 February 2010; accepted 21 March 2010; published online 4 May 2010)

The ability to calculate flows generated by oscillating cylinders immersed in fluid is a cornerstone in micro- and nanodevice development. In this article, we present a detailed theoretical analysis of the hydrodynamic load experienced by an oscillating rigid cylinder, of arbitrary rectangular cross section, that is immersed in an unbounded viscous fluid. We also consider the formal limit of inviscid flow for which exact analytical and asymptotic solutions are derived. Due to its practical importance in application to the atomic force microscope and nanoelectromechanical systems, we conduct a detailed assessment of the dependence of this load on the cylinder thickness-to-width ratio. We also assess the validity and accuracy of the widely used infinitely-thin blade approximation. For thin rectangular cylinders of finite thickness, this approximation is found to be excellent for out-of-plane motion, whereas for in-plane oscillations it can exhibit significant error. A database of accurate numerical results for the hydrodynamic load as a function of the thickness-to-width ratio and normalized frequency is also presented, which is expected to be of value in practical application and numerical benchmarking. © *2010 American Institute of Physics*. [doi:10.1063/1.3397926]

I. INTRODUCTION

The dynamic response of elastic beam resonators is used in a host of practical applications, including the ultrasensitive measurement of mass using nanoelectromechanical systems (NEMS)[1–3] and microfluidic devices,[4,5] detection of fluid properties using microcantilever sensors,[6] and force measurement using the atomic force microscope (AFM).[7,8] It is widely recognized that the frequency response of such elastic bodies can depend strongly on the fluid in which they are immersed, and over the past decade there have been a number of theoretical treatments of this problem, with particular emphasis given to cantilever beams.[9–15] Many of these theoretical models are also applicable to elastic beams under different clamp conditions, as discussed in Ref. 16.

Intrinsic to these theoretical treatments is the approximation of the hydrodynamic load at any section along the deforming elastic beam by the two-dimensional flow generated by a corresponding rigid cylinder (of identical cross section and oscillation amplitude), the theoretical basis of which is discussed in Ref. 14. This approximation has been validated by numerous workers using both numerical simulations of the full three-dimensional flow[9] and experiment.[17] In many cases, the oscillating cylinders are considered to be sufficiently thin so as to facilitate the use of a model involving an infinitely thin blade.[9–16] This "infinitely thin" model has found great utility in analyzing practical device behavior and is the basis of many theoretical treatments of cantilever beams immersed in fluids. These include studies of proximity effects to solid surfaces[10,12,18] and hydrodynamic coupling between arrays of micromechanical oscillators.[19] Importantly, however, many devices also possess beams whose thickness-to-width ratio draws into question the validity of this infinitely thin approximation. This is particularly the case in NEMS devices, which can exhibit thicknesses comparable to the beam width.[20–23] No model for this important practical case exists currently, and the precise regime under which the infinitely thin model holds is unknown.

In this article, we investigate the practical case of an oscillating (rigid) cylinder of arbitrary rectangular cross section immersed either in an inviscid or a viscous fluid, and thus address this important gap in the literature. The following terminology shall be used: (i) a "beam" shall henceforth refer to an elastic (deformable) beam, (ii) a "cylinder" refers to a rigid cylinder, the cross section of which is arbitrary, and (iii) a "blade" is a rectangular cylinder of zero thickness.

Developments in NEMS technologies have also facilitated the use of vibration modes not commonly addressed in the literature, e.g., see Bargatin *et al.*[21] who studied both the in-plane and out-of-plane motions of moderately thin silicon-carbide beams. These devices were actuated thermoelastically at room temperature and their motion detected piezoresistively.[21] Such strain sensing allows for great flexibility in detection, and thus operation using a wider range of modes than that achievable using more conventional detection schemes, such as optical interferometry and optical lever sensing. Analysis of the in-plane oscillation of thin beams in viscous fluids is an outstanding problem that is critical to understanding the operation of these new technologies.

We systematically study the oscillation of rectangular cylinders of arbitrary aspect ratio (thickness/width) immersed in unbounded viscous fluids by adopting and extending the boundary integral technique of Tuck.[24] We also consider the limiting cases of an infinitely thin blade, where the direction of motion is in-plane and out-of-plane to the blade surface. The latter case was originally studied numerically by Tuck, and an exact analytical solution to this problem appeared recently.[25] This exact solution will be used as a

[a)]Electronic mail: jsader@unimelb.edu.au.

benchmark to assess the accuracy of the present numerical scheme. We also improve on the original numerical approach of Tuck using the process of Richardson extrapolation.[26] This greatly accelerates convergence and allows achievement of high accuracy in the numerical results while using moderate mesh spacing. The presented database of numerical results (in Sec. III) is expected to facilitate practical application and allow for benchmarking of future analytical and numerical investigations.

The corresponding formal limit of inviscid flow is solved using the method of conformal mapping.[27] An exact analytical solution for the hydrodynamic load is obtained in this case, from which asymptotic results are derived for thin cylinders executing in-plane and out-of-plane oscillations. These results establish that previous heuristic approximations[28–30] for the effect of finite thickness do not exhibit the correct functional forms, as we shall discuss.

Importantly, we find that use of the infinitely thin approximation yields accurate results for out-of-plane motion of moderately thin rectangular cylinders over a large range of aspect ratios (thickness/width). Conversely, in-plane motion of such cylinders is found to be poorly described by the infinitely thin model. The underlying physical mechanisms giving rise to this differing behavior are explored.

The findings of this article have significant implications to AFM cantilever characterization methods that assume an infinitely thin geometry,[31–35] and NEMS devices which are intrinsically capable of probing both in-plane and out-of-plane motion sensing,[21] as we shall discuss. The present theoretical model allows for calculation of both inertial and dissipative forces generated by the fluid, and is thus expected to find utility in a host of applications involving oscillating elastic beam resonators.

We begin with the principal underlying assumptions of the model in Sec. II. A short review of the boundary integral method of Tuck[24] is then presented, which is followed by its application to a cylinder of arbitrary rectangular cross section. Use of Richardson extrapolation in this method is then discussed. Results arising from these numerical investigations are presented in Sec. III and their implications explored. Solutions for infinitely thin blades undergoing in-plane and out-of-plane oscillations, and exact analytical and asymptotic solutions for inviscid flow of a rectangular cylinder of arbitrary aspect ratio, are relegated to the Appendixes A and B.

II. THEORETICAL MODEL

A schematic diagram of the cylinder cross section is given in Fig. 1(a). The cylinder is immersed in an unbounded quiescent fluid, and the flow problem is assumed to satisfy the following constraints:

(1) The cylinder is assumed to be of infinite extent perpendicular to its cross section, i.e., in the x-direction;
(2) the cross section of the cylinder is rectangular and uniform along its length;
(3) the cylinder is executing oscillations in the y-direction, normal to its longitudinal axis;
(4) the oscillation amplitude is small, so that the Navier–Stokes equation can be linearized; see Ref. 14 for a discussion of the practical implications of this assumption.

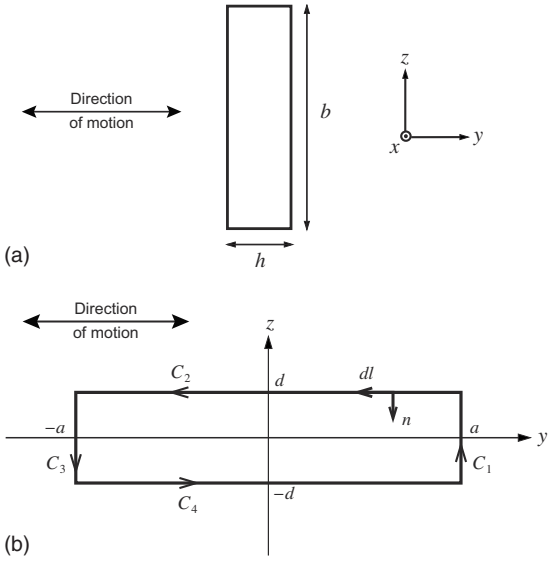

FIG. 1. (a) Schematic diagram showing the cross section of the rectangular cylinder. The origin of the coordinate system is located at the geometric center of the cylinder cross section. (b) Figure showing integration contour and dimensions used in boundary integral formulation for the oscillation of a rectangular cylinder of finite thickness. The origin of the coordinate system is located at the geometric center of the cross section.

In contrast to previous theoretical models,[9–15] the aspect ratio h/b is taken to be arbitrary; see Fig. 1(a). The fluid is also assumed to be incompressible, which is a valid approximation in many cases of practical interest;[14] for a discussion of compressibility effects, see Ref. 16.

Since we are interested in the flow generated by small amplitude oscillations of the cylinder, we take the Fourier transform of the incompressible linearized Navier–Stokes equations, yielding

$$\nabla \cdot \hat{\mathbf{u}} = 0, \quad -\nabla \hat{p} + \mu \nabla^2 \hat{\mathbf{u}} = -i\rho\omega\hat{\mathbf{u}}, \tag{1}$$

where

$$\hat{Z} = \int_{-\infty}^{\infty} Z e^{i\omega t} dt$$

for any function of time Z, and i is the usual imaginary unit. Henceforth, we shall omit this superfluous "hat" notation, since all results shall be presented in the frequency domain. The vector $\mathbf{u}$ is the velocity field, p is the pressure, ρ is the density of the fluid, and μ its shear viscosity.

The hydrodynamic force per unit length, F_{hydro}, experienced by the cylinder can be nondimensionalized[14] to give

$$F_{\text{hydro}} = \frac{\pi}{4}\rho\omega^2 X^2 \Gamma(\omega) W_{\text{cyl}}, \tag{2}$$

where $\Gamma(\omega)$ is the "hydrodynamic function" which is a complex-valued dimensionless function, and W_{cyl} is the displacement amplitude of the cylinder in the same direction as the force, i.e., in the y-direction. The constant X is the dominant length scale of the flow, which is taken to be $\max(h,b)$,

see Fig. 1(a). The real and imaginary components of the hydrodynamic function represent the added apparent mass (inertial) and dissipative (damping) components of the load.

Tuck[24] gave a two-dimensional streamfunction representation of Eq. (1) for the flow generated by a cylinder of arbitrary cross section executing small amplitude oscillations in an unbounded quiescent fluid,

$$\psi = \int_C \left[\psi G_n - \psi_n \Omega - \zeta \Psi_n + \frac{1}{\mu} p \Psi_l \right] dl, \tag{3}$$

where the contour C coincides with the surface of the cylinder and encompasses the entire fluid domain.[18,24] The streamfunction ψ satisfies $\nabla^4 \psi = \alpha^2 \nabla^2 \psi$. In Eq. (3), the subscripts l and n represent the derivatives tangential and normal to C, respectively, and ζ is the component of the vorticity in the x-direction. The function Ψ is the corresponding Green's function for the streamfunction, and thus satisfies $\nabla^4 \Psi - \alpha^2 \nabla^2 \Psi = \delta$. A solution to this equation is[24]

$$\Psi = -\frac{1}{2\pi\alpha^2}[\log(\alpha R) + K_0(\alpha R)], \tag{4}$$

where K_0 is the modified Bessel function of the third kind, zeroth order.[36] In Eq. (4), $\alpha^2 = -i\omega/\nu$ and $R = \sqrt{(y-y')^2 + (z-z')^2}$. The parameter ν is the kinematic viscosity of the fluid and ω is the angular frequency at which the cylinder oscillates. We also have

$$G = \frac{1}{2\pi}\log(\alpha R), \quad \Omega = -\frac{1}{2\pi} K_0(\alpha R),$$

where $\nabla^2 \Omega - \alpha^2 \Omega = \delta(y-y')\delta(z-z')$ and $\Psi = (1/\alpha^2)(\Omega - G)$. The Green's function G satisfies the two dimensional equation, $\nabla^2 G = \delta(y-y')\delta(z-z')$.

It is convenient to pose the problem in the noninertial reference frame of the cylinder, since its surface then constitutes a single streamline; the value of the corresponding streamfunction at the cylinder surface is set to zero. Physically, this reference frame corresponds to a stationary cylinder immersed in an unbounded fluid that is oscillating at angular frequency ω. In this noninertial reference frame, the reduced fluid velocity $\bar{\mathbf{u}}$ is related to the true fluid velocity $\mathbf{u}$ by

$$\mathbf{u} = \bar{\mathbf{u}} + \mathbf{u}_{\mathrm{cyl}}, \tag{5}$$

where $\mathbf{u}_{\mathrm{cyl}}$ is the true velocity of the cylinder surface. The "overscore" shall henceforth refer to reduced variables in this noninertial frame of reference.

The corresponding boundary conditions for the reduced velocity are

$$\bar{\mathbf{u}} = \begin{cases} \mathbf{0}, & \text{at cylinder surface (no-slip)}, \\ -\mathbf{u}_{\mathrm{cyl}}, & \text{at infinity}. \end{cases} \tag{6}$$

Substituting Eq. (5) into Eq. (1) then yields

$$-i\rho\omega\bar{\mathbf{u}} = -\nabla\bar{p} + \mu\nabla^2\bar{\mathbf{u}}, \tag{7}$$

where the reduced pressure $\bar{p}$ is related to the true pressure p by

$$\bar{p} = p - i\rho\omega U_{\mathrm{cyl}} y, \tag{8}$$

and U_{cyl} is the y-component of the cylinder velocity, as the cylinder is taken to be oscillating in this direction—this choice is arbitrary and the z-direction could have been equivalently chosen. The governing flow equation remains unchanged except for the inclusion of an extra body force term due to use of a noninertial frame of reference, as specified in Eq. (8).

Following the boundary integral formulation of Tuck[24] for the reduced governing equation, Eq. (7), the streamfunction in this noninertial reference frame then satisfies

$$\bar{\psi}(y',z') = -U_{\mathrm{cyl}} z' + \int_{C_{\mathrm{cyl}}} \left[-\bar{\zeta}\Psi_n + \frac{1}{\mu}\bar{p}\Psi_l \right] dl, \tag{9}$$

where we have used the fact that $\bar{\psi}$ and $\bar{\psi}_n$ are both identically zero at the cylinder surface. The integral in Eq. (9) is the disturbance flow due to the presence of the cylinder. In the absence of the cylinder, the integral in Eq. (9) vanishes and we are left with the streamfunction corresponding to uniform (rigid-body) oscillatory flow.

The vector force $\mathbf{F}$ acting on any three-dimensional body with surface S, moving in any manner in an unbounded quiescent incompressible fluid, is given by[24]

$$\mathbf{F} = \int_S [-p d\mathbf{S} + \mu\boldsymbol{\zeta} \times d\mathbf{S}].$$

The component of the force in the y-direction (the direction of motion) is then

$$F_y = \mathbf{j}\cdot\mathbf{F} = \int_{C_{\mathrm{cyl}}} [-p dz + \mu\zeta dy], \tag{10}$$

where C_{cyl} is the cylinder surface. Comparing Eq. (10) with Eq. (2), and noting that $U_{\mathrm{cyl}} = -i\omega W_{\mathrm{cyl}}$, we obtain the required result for the hydrodynamic function in the y-direction,

$$\Gamma(\omega) = -\frac{4i}{\pi\rho\omega X^2 U_{\mathrm{cyl}}} \int_{C_{\mathrm{cyl}}} [-p dz + \mu\zeta dy]. \tag{11}$$

Since the problem is linear, Eq. (11) is independent of the oscillation amplitude.

A. Cylinder of arbitrary rectangular cross section

We now apply the above formulation to a cylinder of rectangular cross section executing small amplitude oscillations in the y-direction under the conditions detailed above. The contour of integration used in the boundary integral formulation, Eq. (9), is illustrated in Fig. 1(b) and specified by $C_{\mathrm{cyl}} = C_1 + C_2 + C_3 + C_4$. The side dimensions of the cylinder have been denoted a and d, and are related to the thickness h and width b, respectively, by a factor of 1/2. This allows for the same oscillation direction to be used throughout, as specified in Fig. 1(b), while choosing a different dominant length scale corresponding to the width or thickness. This notation is chosen purely for convenience. Although the mo-

tion of the beam is restricted to the y-direction, we can investigate either in-plane or out-of-plane motion simply by choosing $h>b$ or $h<b$, respectively.

Henceforth, the faces C_1 and C_2 as depicted in Fig. 1(b) will be referred to as the *leading* and *side* faces, respectively. We consider the reduced problem and work in the noninertial reference frame of the cylinder, i.e., the cylinder is stationary and the unbounded fluid is oscillating. Without loss of generality, we initially consider $2a$ to be the dominant length scale, as illustrated in Fig. 1(b). The appropriate boundary conditions for the fluid at the cylinder surface are given in Eq. (6). We also make use of the fact that the pressure on the surface of the cylinder is symmetric about the y-axis and antisymmetric about the z-axis. Conversely, the vorticity at the surface is antisymmetric about the y-axis and symmetric about the z-axis. These symmetry conditions can be easily derived from the Navier–Stokes equation.[25] The aspect ratio (thickness/width) of the cylinder is defined as

$$A \equiv \frac{a}{d} = \frac{h}{b}. \tag{12}$$

Scaling the spatial dimensions by a, we obtain $\xi=y/a$ and $\chi=z/a$. From this scaling, it follows that $\xi\in[-1,1]$ and $\chi\in[-1/A,1/A]$. We also define the dimensionless frequency, $\beta=\omega a^2/\nu$; this parameter is also commonly referred to as the Reynolds number, inverse Stokes parameter, or Womersley number. The reduced pressure and vorticity are scaled according to

$$P_1(\chi) = \frac{a}{\mu U_{\mathrm{cyl}}}\bar{p}_1(z), \quad \Lambda_1(\chi) = \frac{a}{U_{\mathrm{cyl}}}\bar{\zeta}_1(z),$$
$$P_2(\xi) = \frac{a}{\mu U_{\mathrm{cyl}}}\bar{p}_2(y), \quad \Lambda_2(\xi) = \frac{a}{U_{\mathrm{cyl}}}\bar{\zeta}_2(y). \tag{13}$$

Upon application of the appropriate boundary conditions, Eq. (9) yields the following pair of coupled integral equations:

$$\begin{aligned} 1 = &\int_{-1/A}^{1/A} [\Lambda_1(\chi)(\tilde{\Psi}_{\xi\chi'}|_{\xi=1} - \tilde{\Psi}_{\xi\chi'}|_{\xi=-1}) \\ &+ P_1(\chi)(\tilde{\Psi}_{\chi\chi'}|_{\xi=1} + \tilde{\Psi}_{\chi\chi'}|_{\xi=-1})]d\chi \\ &+ \int_{-1}^{1} [\Lambda_2(\xi)(\tilde{\Psi}_{\chi\chi'}|_{\chi=1/A} + \tilde{\Psi}_{\chi\chi'}|_{\chi=-1/A}) \\ &+ P_2(\xi)(\tilde{\Psi}_{\xi\chi'}|_{\chi=-1/A} - \tilde{\Psi}_{\xi\chi'}|_{\chi=1/A})]d\xi, \end{aligned} \tag{14}$$

$$\begin{aligned} 0 = &\int_{-1/A}^{1/A} [\Lambda_1(\chi)(\tilde{\Psi}_{\xi\xi'}|_{\xi=1} - \tilde{\Psi}_{\xi\xi'}|_{\xi=-1}) \\ &+ P_1(\chi)(\tilde{\Psi}_{\chi\xi'}|_{\xi=1} + \tilde{\Psi}_{\chi\xi'}|_{\xi=-1})]d\chi \\ &+ \int_{-1}^{1} [\Lambda_2(\xi)(\tilde{\Psi}_{\chi\xi'}|_{\chi=1/A} + \tilde{\Psi}_{\chi\xi'}|_{\chi=-1/A}) \\ &+ P_2(\xi)(\tilde{\Psi}_{\xi\xi'}|_{\chi=-1/A} - \tilde{\Psi}_{\xi\xi'}|_{\chi=1/A})]d\xi, \end{aligned} \tag{15}$$

where the right hand sides of the above equations are evaluated on the faces of the cylinder. These equations contain the nondimensionalized Green's function $\tilde{\Psi}=\Psi/a^2$.

To solve Eqs. (14) and (15), we discretize the integrals to obtain a system of linear equations. The expected square-root singularities in the pressure and vorticity at the corners of the cylinder cross section[24] are handled using the quadrature $\chi_m=-(1/A)\cos(\pi m/M)$ and $\xi_n=-\cos(\pi n/N)$, where $m=0,1,\ldots,M$ and $n=0,1,\ldots,N$. Provided the discretization is sufficiently fine, the pressure and vorticity can then be approximated to be constant in each interval, i.e., $P_1(\chi)=P_{1,m}$ and $\Lambda_1(\chi)=\Lambda_{1,m}$ for $\chi_m<\chi<\chi_{m+1}$ and $P_2(\xi)=P_{2,n}$ and $\Lambda_2(\xi)=\Lambda_{2,n}$ for $\xi_n<\xi<\xi_{n+1}$. Equations (14) and (15) thus become

$$\begin{aligned} &\sum_{m=0}^{M-1} [\Lambda_{1,m}I_1(\xi',\chi') + P_{1,m}I_2(\xi',\chi')] \\ &\quad + \sum_{n=0}^{N-1} [\Lambda_{2,n}I_3(\xi',\chi') + P_{2,n}I_4(\xi',\chi')] = 1, \end{aligned} \tag{16}$$

$$\begin{aligned} &\sum_{m=0}^{M-1} [\Lambda_{1,m}J_1(\xi',\chi') + P_{1,m}J_2(\xi',\chi')] \\ &\quad + \sum_{n=0}^{N-1} [\Lambda_{2,n}J_3(\xi',\chi') + P_{2,n}J_4(\xi',\chi')] = 0, \end{aligned} \tag{17}$$

where

$$\begin{aligned} I_1(\xi',\chi') &= \int_{\chi_m}^{\chi_{m+1}} (\tilde{\Psi}_{\xi\chi'}|_{\xi=1} - \tilde{\Psi}_{\xi\chi'}|_{\xi=-1})d\chi, \\ I_2(\xi',\chi') &= \int_{\chi_m}^{\chi_{m+1}} (\tilde{\Psi}_{\chi\chi'}|_{\xi=1} + \tilde{\Psi}_{\chi\chi'}|_{\xi=-1})d\chi, \\ I_3(\xi',\chi') &= \int_{\xi_n}^{\xi_{n+1}} (\tilde{\Psi}_{\chi\chi'}|_{\chi=1/A} + \tilde{\Psi}_{\chi\chi'}|_{\chi=-1/A})d\xi, \\ I_4(\xi',\chi') &= \int_{\xi_n}^{\xi_{n+1}} (\tilde{\Psi}_{\xi\chi'}|_{\chi=-1/A} - \tilde{\Psi}_{\xi\chi'}|_{\chi=1/A})d\xi, \\ J_1(\xi',\chi') &= \int_{\chi_m}^{\chi_{m+1}} (\tilde{\Psi}_{\xi\xi'}|_{\xi=1} - \tilde{\Psi}_{\xi\xi'}|_{\xi=-1})d\chi, \\ J_2(\xi',\chi') &= \int_{\chi_m}^{\chi_{m+1}} (\tilde{\Psi}_{\chi\xi'}|_{\xi=1} + \tilde{\Psi}_{\chi\xi'}|_{\xi=-1})d\chi, \\ J_3(\xi',\chi') &= \int_{\xi_n}^{\xi_{n+1}} (\tilde{\Psi}_{\chi\xi'}|_{\chi=1/A} + \tilde{\Psi}_{\chi\xi'}|_{\chi=-1/A})d\xi, \\ J_4(\xi',\chi') &= \int_{\xi_n}^{\xi_{n+1}} (\tilde{\Psi}_{\xi\xi'}|_{\chi=-1/A} - \tilde{\Psi}_{\xi\xi'}|_{\chi=1/A})d\xi. \end{aligned} \tag{18}$$

To close the system, we then demand that Eqs. (16) and (17) hold at the midpoint of each segment on the discretized intervals, i.e., $(\xi',\chi')=(\xi'_k,1/A)=([\xi_k+\xi_{k+1}]/2,1/A)$ and $(\xi',\chi')=(1,\chi'_j)=(1,[\chi_j+\chi_{j+1}]/2)$ for $k=0,\ldots,N-1$ and $j=0,\ldots,M-1$. Applying these conditions to Eqs. (16) and (17) yields a matrix-vector equation

$$\begin{bmatrix} [I_1(1,\chi'_j)]_{jm} & [I_2(1,\chi'_j)]_{jm} & [I_3(1,\chi'_j)]_{jn} & [I_4(1,\chi'_j)]_{jn} \\ \left[I_1\left(\xi'_k,\frac{1}{A}\right)\right]_{km} & \left[I_2\left(\xi'_k,\frac{1}{A}\right)\right]_{km} & \left[I_3\left(\xi'_k,\frac{1}{A}\right)\right]_{kn} & \left[I_4\left(\xi'_k,\frac{1}{A}\right)\right]_{kn} \\ [J_1(1,\chi'_j)]_{jm} & [J_2(1,\chi'_j)]_{jm} & [J_3(1,\chi'_j)]_{jn} & [J_4(1,\chi'_j)]_{jn} \\ \left[J_1\left(\xi'_k,\frac{1}{A}\right)\right]_{km} & \left[J_2\left(\xi'_k,\frac{1}{A}\right)\right]_{km} & \left[J_3\left(\xi'_k,\frac{1}{A}\right)\right]_{kn} & \left[J_4\left(\xi'_k,\frac{1}{A}\right)\right]_{kn} \end{bmatrix} \begin{bmatrix} \mathbf{\Lambda}_1 \\ \mathbf{P}_1 \\ \mathbf{\Lambda}_2 \\ \mathbf{P}_2 \end{bmatrix} = \begin{bmatrix} 1 \\ 1 \\ \vdots \\ 1 \\ 0 \\ 0 \\ \vdots \\ 0 \end{bmatrix}. \tag{19}$$

Interestingly, the majority of integrals in Eq. (18) can be evaluated analytically without recourse to numerical methods by noting that $\tilde{\Psi}_{\xi\chi'}(\xi,\chi;\xi',\chi')=\tilde{\Psi}_{\chi\xi'}(\xi,\chi;\xi',\chi')$, $\tilde{\Psi}_{\xi'}(\xi,\chi;\xi',\chi')=-\tilde{\Psi}_{\xi}(\xi,\chi;\xi',\chi')$, and $\tilde{\Psi}_{\chi'}(\xi,\chi;\xi',\chi')=-\tilde{\Psi}_{\chi}(\xi,\chi;\xi',\chi')$. All but two of the integrals in Eq. (18) can be evaluated analytically through use of these symmetry conditions. The integrals I_3 and J_1 are more stubborn and we must resort to numerical integration. MATHEMATICA® was used in construction of the matrix system, Eq. (19), and for numerical evaluation of all functions.

Calculation of the hydrodynamic function follows directly from Eq. (11) in conjunction with the computed values of the pressure and vorticity. Recalling that $\beta=\omega a^2/\nu$, we find

$$\Gamma(\omega)=\frac{2i}{\pi\beta}\left(\int_{-1/A}^{1/A}P(\chi)d\chi+\int_{-1}^{1}\Lambda(\xi)d\xi\right)-\frac{4}{\pi A}, \tag{20}$$

whose discrete form is

$$\Gamma(\omega)=\frac{2i}{\pi\beta}\left(\sum_{m=0}^{M-1}(\chi_{m+1}-\chi_m)P_m+\sum_{n=0}^{N-1}(\xi_{n+1}-\xi_n)\Lambda_n\right)-\frac{4}{\pi A}+O(N^{-2}), \tag{21}$$

where the constant term involving the aspect ratio A arises from the choice of a noninertial reference frame in the formulation.

Clearly, if $2d$ is chosen as the dominant length scale then Eq. (21) can be trivially modified. Since the dominant length scale will be chosen to be the larger of $2a$ and $2d$, Eq. (21) can be generalized to give

$$\Gamma(\omega)=\frac{2i}{\pi\beta}\left(\sum_{m=0}^{M-1}(\chi_{m+1}-\chi_m)P_m+\sum_{n=0}^{N-1}(\xi_{n+1}-\xi_n)\Lambda_n\right)-\frac{4}{\pi}\min\left(A,\frac{1}{A}\right)+O(N^{-2}), \tag{22}$$

where

$$\beta=\frac{\omega\kappa^2}{\nu} \tag{23}$$

and $\kappa=\max(a,d)$. In presenting Eqs. (21) and (22), we have implicitly assumed that $M\geq N$ so that the dominant discretization error is of order $O(N^{-2})$. Numerical simulations in Sec. III are undertaken with $M=N$.

B. Richardson extrapolation

We note that the expression for $\Gamma(\omega)$ in Eq. (22) possesses a discretization error of order $O(N^{-2})$; this results from use of the midpoint rule.[26] Since this dominant error behavior is known, we employ the method of Richardson extrapolation to accelerate convergence using a sequence of solutions for various N. This facilitates accurate numerical solutions while using modest mesh sizes and hence moderate values of N. The process of Richardson extrapolation is discussed by Hornbeck[26] and summarized here.

We begin with n estimates $\Gamma_{1,i}$ $(i=1,\ldots,n)$ for Γ, computed on a series of meshes for which N differs by a factor of 2, i.e., $N=2^{i-1}N_0$, where N_0 is a positive integer. The following extrapolation formula is then used to estimate and remove the dominant error term in these initial results:

$$\Gamma_{l,k}=\frac{2^{p(l-1)}\Gamma_{l-1,k+1}-\Gamma_{l-1,k}}{2^{p(l-1)}-1}, \tag{24}$$

where the parameter l is the iteration number and p is the inverse power of the dominant error term, which in our case is $p=2$.

This yields $n-1$ new estimates for Γ, each with the dominant error term removed. Equation (24) is then used

recursively until only a single value for Γ remains. For example, choosing four values of N (and hence Γ) with an associated error of $O(N^{-2})$ results in a single value for Γ whose dominant error is $O(N^{-8})$ after three cycles of iteration. This iteration procedure is used in Sec. III to greatly accelerate convergence of numerical results.

III. RESULTS AND DISCUSSION

Results shall now be presented for cylinders of arbitrary rectangular cross section and infinitely thin blades executing in-plane and out-of-plane oscillations; see Appendixes A 1 and A 2 for solutions to the latter cases. The solution for inviscid flow is given in Appendix B. We study the vorticity and pressure generated at the surfaces of these two-dimensional bodies and examine the physical implications of these results to the net hydrodynamic load. We also present accurate numerical results for the hydrodynamic function $\Gamma(\omega)$ in Table I, which is expected to be of significant value in practical applications and numerical benchmarking of future studies.

A. Infinitely thin blade

1. Out-of-plane oscillation

We first consider an infinitely thin blade executing out-of-plane oscillations in a viscous fluid. The boundary integral method of Tuck[24] is used to solve this problem, an outline of which is given in Appendix A 2. Since the quadrature scheme used in this method is identical to that in Sec. II A, the associated discretization error is also of order $O(N^{-2})$. Consequently, the method of Richardson extrapolation is directly applicable, and the aim of this section is to demonstrate its utility in accelerating convergence. This is particularly important since computational time increases as N^2. The exact analytical solution presented in Ref. 25 is used to benchmark this study.

We focus on a single value of β to demonstrate the salient features of this extrapolation procedure. In Fig. 2, we present values of the hydrodynamic function for $\beta=1/4$ and various N; this value of β is chosen since accurate numerical data (correct to six significant figures) are given in Ref. 25: $\Gamma_{\text{exact}}=6.643\,52+10.8983i$. The "computed" column in Fig. 2 contains raw output from the Tuck solution, whereas data in the columns to the right are obtained using the process of Richardson extrapolation, i.e., Eq. (24).

It is evident from Fig. 2 that use of Richardson extrapolation greatly accelerates convergence for a given value of N. In particular, note that Γ is accurately computed to six significant figures using raw results for $N=10$, 20, 40, and 80 and the Richardson extrapolation procedure. This contrasts to the raw solution for $N=320$ that exhibits accuracy to only five significant figures.

As mentioned above, the computational time taken to construct the matrix system grows with N^2 due to the number of entries in the resultant matrix. Use of a minimal value of N is thus highly desirable for computational efficiency. For out-of-plane oscillations of an infinitely thin blade, the matrix entries can be evaluated analytically, thus facilitating computational speed. However, for rectangular cylinders of finite thickness and in-plane oscillations of infinitely thin blades, some integrals require numerical evaluation; see Eqs. (18) and (A8). This greatly increases computational time, and efficiency improvements through use of Richardson extrapolation are thus essential to achieving highly accurate solutions.

2. In-plane oscillation

Next, we examine the in-plane oscillations of an infinitely thin blade in a viscous fluid, the solution method of which is given in Appendix A 1. Note that the primary fluid variable involved in determining the hydrodynamic load is the vorticity at the blade surface; the pressure does not contribute to the load. The resulting matrix-vector system in Eq. (A7) can be readily constructed and solved using MATHEMATICA®, yielding the vorticity at the corresponding mesh points. Although an exact analytical solution to this flow problem does not exist, we can analytically examine the solution behavior in the asymptotic limit of $\beta \gg 1$. In this asymptotic limit, thin viscous boundary layers exist at the blade surfaces, the flow field of which is given by Stokes' second problem for the oscillations of an infinite half-space in an unbounded fluid;[37] effects associated with the blade edges exhibit a comparatively negligible effect. This yields the following asymptotic result for the scaled vorticity at the blade surface (away from the edges):

$$\Lambda \sim -i\sqrt{i\beta}, \quad \beta \gg 1. \tag{25}$$

Figure 3 shows the vorticity distribution for various values of β and the asymptotic solution for $\beta \gg 1$. Since the vorticity is an even function of ξ, results are presented for $\xi \in [0,1]$ only.

Note that both the real and imaginary components of the vorticity approach the asymptotic solution in Eq. (25) as β increases. We emphasize that the asymptotic solution, Eq. (25), is not applicable in the immediate vicinity of the blade edges. Viscous boundary layers in these regions can no longer be considered thin and square root singularities are observed in the full numerical solution, as expected. These singularities are inherently captured by the choice of numerical quadrature, as discussed in Appendix A 1. These results serve to illustrate the validity of the numerical method in calculating the vorticity distribution across the faces of the blade.

In contrast to the out-of-plane case, the integrals involved in constructing the matrix system for in-plane oscillations do not permit analytical evaluation. Since the discretization error is also of order $O(N^{-2})$, the Richardson extrapolation procedure detailed above is used to accelerate convergence and improve computational efficiency. This is applied only to numerical results for the hydrodynamic function in order to achieve highly accurate solutions, since differences in the vorticity are indiscernible in Fig. 3.

Results for the hydrodynamic function as a function of β are given in Fig. 4. As expected, these numerical results approach the required asymptotic solution as $\beta \to \infty$, providing validation of the full numerical solution. Importantly, we find that reducing β enhances the hydrodynamic load experienced

TABLE I. Hydrodynamic function Γ as a function of dimensionless frequency β and aspect ratio A. Results are accurate to the number of significant figures shown. (a) Real component; $\beta \to \infty$ results have been computed using the inviscid solution in Appendix B. (b) Imaginary component.

		A												
	$\log_{10}(\beta)$	0	1/50	1/20	1/10	1/5	1/2	1	2	5	10	20	50	∞
(a)	−3	212.184	213.310	214.977	217.701	222.978	237.780	260.256	207.210	169.667	154.616	145.909	139.855	134.720
	−2.5	91.6984	92.2467	93.0601	94.3924	96.9808	104.295	115.542	88.9011	70.8173	63.7655	59.7404	56.9653	54.6258
	−2	41.6417	41.9209	42.3363	43.0185	44.3487	48.1380	54.0391	39.8564	30.6996	27.2460	25.3060	23.9817	22.8730
	−1.5	20.1196	20.2683	20.4907	20.8572	21.5753	23.6370	26.8847	18.8235	13.9212	12.1457	11.1673	10.5072	9.958 83
	−1	10.4849	10.5677	10.6926	10.8998	11.3080	12.4883	14.3601	9.435 36	6.646 06	5.685 11	5.168 01	4.824 11	4.540 93
	−0.5	5.966 55	6.014 67	6.088 71	6.212 79	6.458 97	7.173 28	8.300 52	5.047 39	3.352 15	2.803 94	2.517 94	2.331 26	2.179 27
	0	3.733 87	3.763 44	3.810 63	3.890 99	4.051 54	4.513 68	5.222 20	2.890 30	1.783 22	1.453 06	1.288 07	1.183 27	1.099 43
	0.5	2.565 48	2.585 63	2.619 59	2.678 32	2.795 15	3.119 07	3.585 31	1.776 17	0.994 540	0.783 333	0.684 003	0.623 512	0.576 619
	1	1.918 34	1.935 09	1.964 37	2.014 50	2.110 58	2.356 65	2.682 70	1.177 79	0.580 514	0.435 349	0.372 208	0.336 075	0.309 503
	1.5	1.545 54	1.562 85	1.592 47	1.640 69	1.726 87	1.927 85	2.175 51	0.848 104	0.357 549	0.249 659	0.206 674	0.184 001	0.168 601
	2	1.326 33	1.346 58	1.378 82	1.427 57	1.508 44	1.684 37	1.888 62	0.663 505	0.235 193	0.148 772	0.117 201	0.102 069	0.092 877 9
	2.5	1.195 77	1.2202	1.2555	1.3051	1.3833	1.5459	1.7259	0.559 39	0.167 03	0.093 131	0.068 128	0.057 273	0.051 564 8
	3	1.117 46	1.1465	1.1843	1.2346	1.3117	1.4670	1.6336	0.500 51	0.128 74	0.062 098	0.040 918	0.032 516	0.028 774 5
	∞	1	1.045 51	1.088 16	1.140 64	1.217 03	1.363 68	1.513 17	0.340 920	0.048 681 0	0.011 406 4	0.002 720 41	0.000 418 204	0
(b)	−3	1018.72	1021.37	1025.29	1031.66	1043.88	1077.39	1126.32	1008.65	915.159	874.583	850.149	832.704	817.599
	−2.5	374.276	375.392	377.040	379.721	384.873	399.079	420.012	370.057	331.318	314.778	304.899	297.884	291.835
	−2	140.659	141.144	141.862	143.031	145.284	151.534	160.848	138.825	122.228	115.278	111.167	108.266	105.776
	−1.5	54.4049	54.6253	54.9508	55.4818	56.5079	59.3754	63.7087	53.5749	46.1812	43.1534	41.3825	40.1420	39.0836
	−1	21.8269	21.9314	22.0855	22.3371	22.8247	24.2002	26.3169	21.4324	17.9905	16.6153	15.8210	15.2692	14.8012
	−0.5	9.168 70	9.220 24	9.295 87	9.419 36	9.659 73	10.3480	11.4345	8.96804	7.289 29	6.635 16	6.262 19	6.005 23	5.788 62
	0	4.074 67	4.100 43	4.137 79	4.198 95	4.319 57	4.676 05	5.259 77	3.959 20	3.102 74	2.776 71	2.592 98	2.467 33	2.361 86
	0.5	1.933 66	1.945 52	1.962 56	1.991 30	2.051 07	2.241 27	2.565 35	1.852 52	1.397 90	1.228 68	1.134 29	1.070 13	1.016 39
	1	0.981 710	0.985 312	0.990 956	1.002 55	1.031 57	1.136 34	1.317 68	0.915 797	0.666 095	0.575 374	0.525 354	0.491 568	0.463 359
	1.5	0.527 773	0.526 433	0.526 077	0.529 479	0.543 868	0.602 276	0.703 142	0.474 037	0.333 253	0.283 225	0.256 021	0.237 799	0.222 666
	2	0.296 143	0.291 987	0.289 093	0.289 338	0.296 683	0.328 687	0.384 789	0.253 907	0.173 548	0.145 302	0.130 165	0.120 135	0.111 868
	2.5	0.171 115	0.165 64	0.162 34	0.161 71	0.165 25	0.182 60	0.213 84	0.139 10	0.093 151	0.076 988	0.068 405	0.062 790	0.058 213 4
	3	0.100 688	0.095 021	0.092 307	0.091 476	0.093 044	0.102 47	0.119 87	0.077 266	0.051 022	0.041 760	0.036 840	0.033 652	0.031 090 5

N	*Computed*	*Extrapolated*				
10	6.57971					
20	6.62686	**6.64258**				
40	6.63927	6.64341	**6.64347**			
80	6.64245	6.64351	6.64352	**6.64352**		
160	6.64326	6.64352	6.64352	6.64352	**6.64352**	
320	6.64346	6.64352	6.64352	6.64352	6.64352	**6.64352**

(a)

N	*Computed*	*Extrapolated*				
10	10.8462					
20	10.8849	**10.8978**				
40	10.8949	10.8982	**10.8983**			
80	10.8974	10.8983	10.8983	**10.8983**		
160	10.8981	10.8983	10.8983	10.8983	**10.8983**	
320	10.8982	10.8983	10.8983	10.8983	10.8983	**10.8983**

(b)

FIG. 2. Hydrodynamic function Γ for $\beta=1/4$, (a) real and (b) imaginary components. Richardson extrapolation used to accelerate convergence. Leftmost column gives raw solutions, while columns to its right are the results of Richardson extrapolation.

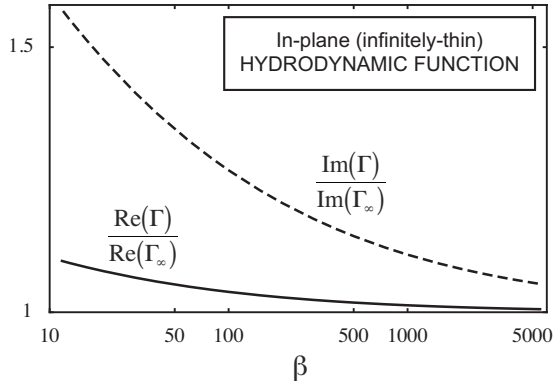

FIG. 4. Real (solid line) and imaginary (dashed line) components of the computed hydrodynamic function. Results are shown as a ratio with the asymptotic solution Γ_∞ (as $\beta\to\infty$) defined in Eq. (A10). Results have been computed with $N=10,20,40,80$ and extrapolated.

by the blade. This is more pronounced in the dissipative component of the load (imaginary part), with the inertial component (real part) exhibiting a relatively weak enhancement. This contrasts to the out-of-plane result, which exhibits similar enhancement in both inertial and dissipative components of the load. This difference appears to be connected to the pressure, which does not contribute to the hydrodynamic load for in-plane motion; the hydrodynamic load for out-of-plane motion is determined solely from the pressure distribution. We will discuss further the relative contributions of the vorticity and pressure in determining the hydrodynamic load in Sec. III B, where we examine the oscillations of a rectangular cylinder of finite thickness.

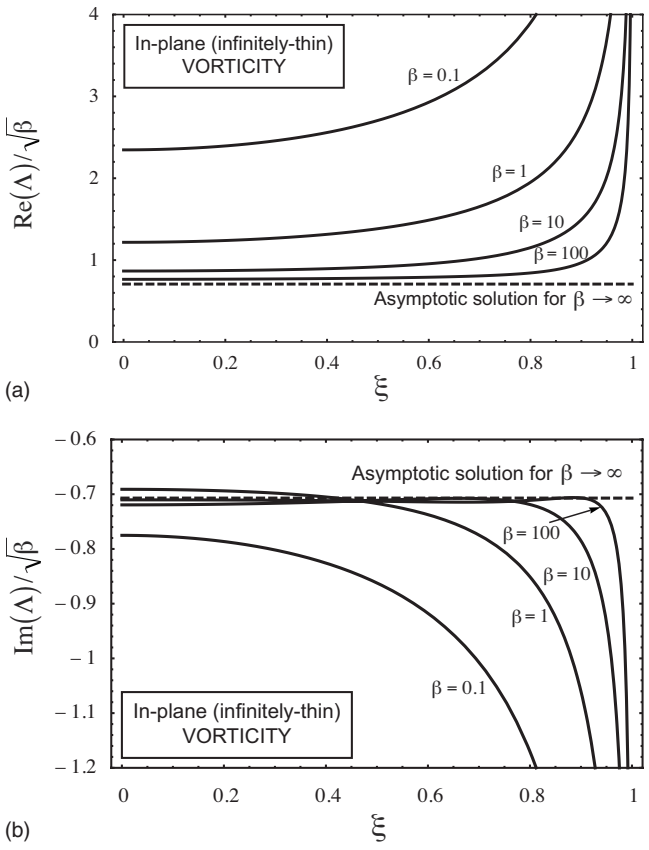

FIG. 3. (a) Real and (b) imaginary components of the vorticity on the top face of the blade. Results have been computed with $N=160$. Dashed lines indicate the asymptotic solution for $\beta\gg1$, whereas solid lines are full numerical solutions.

B. Rectangular cylinder of finite thickness

For a rectangular cylinder of finite thickness, the hydrodynamic load is determined by the pressure and vorticity distributions on the leading and side faces, respectively. We now present results for these quantities that have been obtained using the theory detailed in Sec. II A. We again make use of the inherent symmetry in the cylinder geometry and display results only for half of the physical domain.

Figures 5–8 present results for the pressure and vorticity distributions over the faces of a square cylinder ($A=1$). Both real and imaginary components are presented. Note that the pressure distribution on the leading face differs markedly from that on the side face. As β increases, the pressure distribution away from the edges asymptotes to a limiting solution that corresponds to the inviscid result.

Figure 9 presents the hydrodynamic function versus the dimensionless frequency β for a cylinder of square cross section, i.e., $A=1$. Richardson extrapolation has been employed to accelerate convergence of the numerical solution. Also shown are numerical results for the limiting cases of an infinitely thin blade exhibiting out-of-plane and in-plane motions. Note that scaling of the hydrodynamic load differs in these two limiting cases; one is scaled by the width b, whereas the other is scaled by the thickness h, as discussed above. However, for an aspect ratio of $A=1$, these scalings are identical and results for the square cross section are hence directly comparable to both infinitely thin solutions. Interestingly, we find that the solution for a square cylinder closely follows that of the out-of-plane motion of an infinitely thin blade. While significantly different quantitative behavior is observed for in-plane motion of an infinitely thin blade, similar qualitative variations as a function of β are

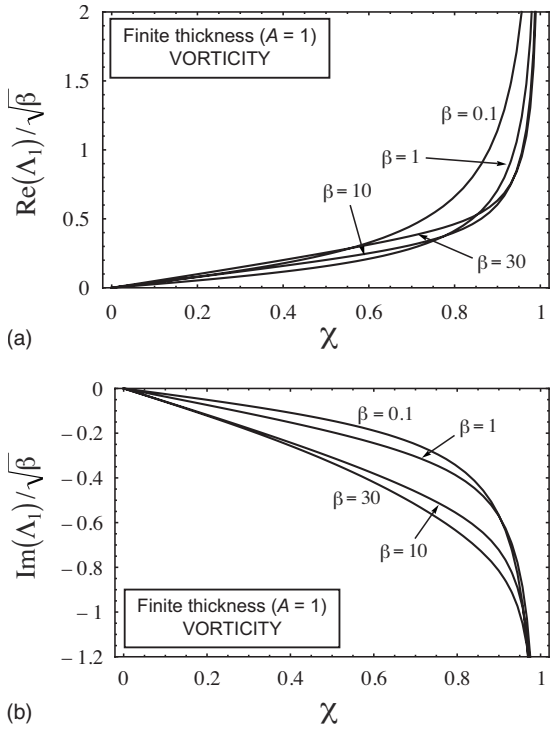

FIG. 5. Vorticity distribution on the *leading face* of a square cylinder ($A=1$). (a) Real component; (b) imaginary component. Results computed with $N=80$.

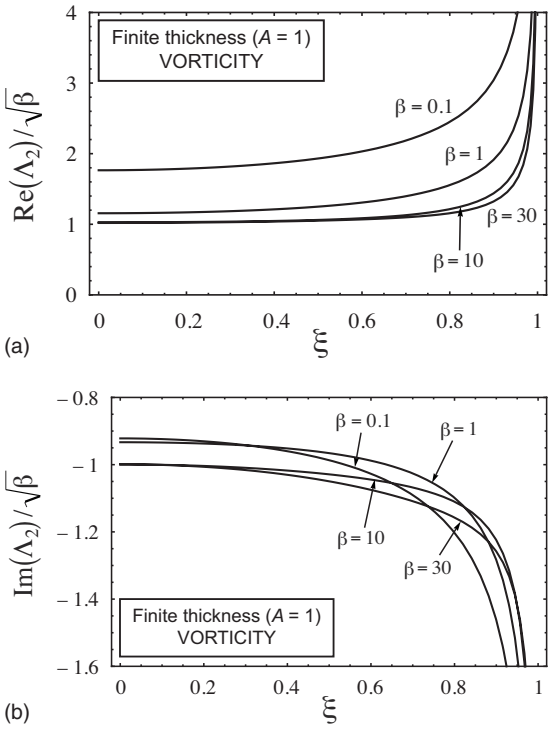

FIG. 7. Vorticity distribution on the *side face* of a square cylinder ($A=1$). (a) Real component; (b) imaginary component. Results computed with $N=80$.

witnessed, i.e., both real and imaginary components of the hydrodynamic load decrease as β increases. This is due to the viscous penetration depth over which vorticity diffuses, decreasing with increasing frequency.

Knowledge of dependence of the hydrodynamic function on the cylinder aspect ratio is of critical practical importance, since many microelectromechanical systems and NEMS devices use rectangular cylinders of arbitrary aspect ratio.[20–23,38] Importantly, it is frequently assumed that a cyl-

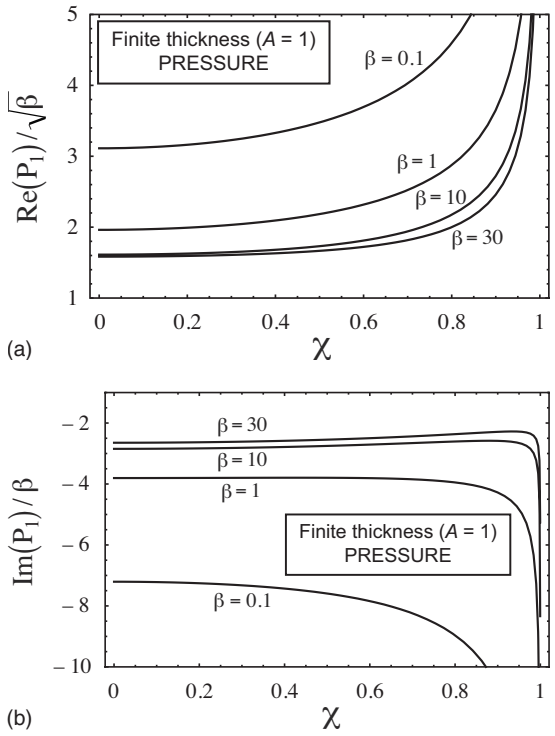

FIG. 6. Pressure distribution on the *leading face* of a square cylinder ($A=1$). (a) Real component; (b) imaginary component. Results computed with $N=80$.

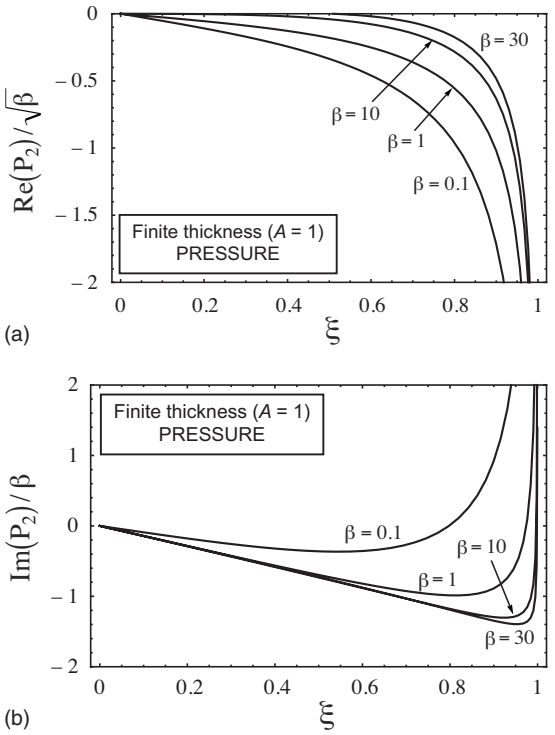

FIG. 8. Pressure distribution on the *side face* of a square cylinder ($A=1$). (a) Real component; (b) imaginary component. Results computed with $N=80$.

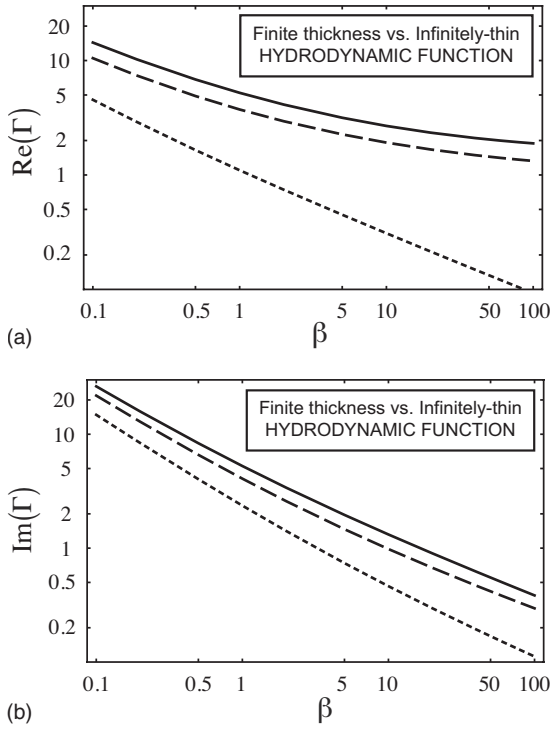

FIG. 9. Hydrodynamic function: (a) real component, (b) imaginary component. Results for $A=1$ (solid line) are shown alongside the infinitely thin results for out-of-plane (dashed line) and in-plane (dotted line) motions.

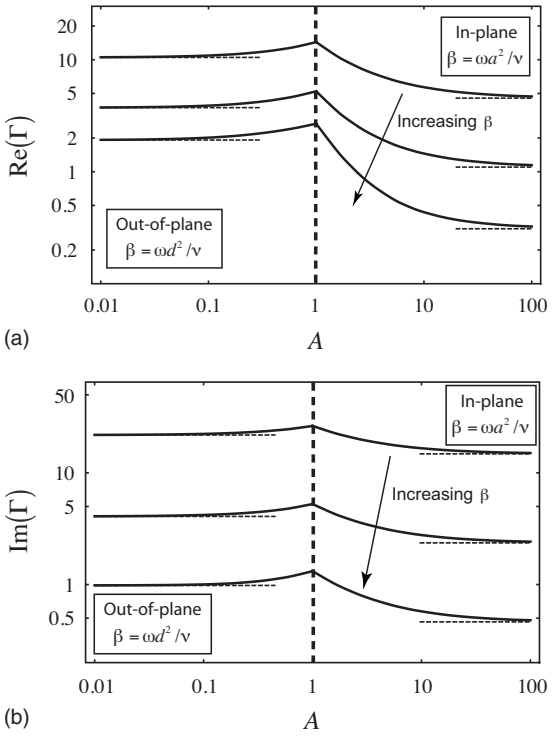

FIG. 10. (a) Real and (b) imaginary components of the hydrodynamic function shown as a function of aspect ratio. Results have been computed for $\beta=1/10,1,10$ and are shown alongside the corresponding infinitely thin limiting cases (horizontal dotted lines).

inder whose thickness is much smaller than its width can be approximated by one which is infinitely thin. The results in Fig. 9 provide some insight into the validity of this approximation. We now fully explore the regime of validity of this commonly used approximation, the results of which are presented in Fig. 10. The limiting cases of an infinitely thin blade executing in-plane ($A\to\infty$) and out-of-plane ($A\to 0$) motions are also presented. Note that the cusps observed in Fig. 10 at $A=1$ are a consequence of different geometric scalings for $A<1$ and $A>1$. From Fig. 10, it is immediately evident that in-plane motion ($A>1$) is much more sensitive to finite cylinder thickness than out-of-plane motion ($A<1$).

The differences observed in Fig. 10 are quantified in Tables II and III for $\beta=10$. Similar results are obtained across the range $1/10<\beta<10$ and are hence not presented here. These tables give the percentage relative difference between the hydrodynamic load for (i) rectangular cylinders of various aspect ratios A and (ii) the corresponding infinitely thin blades. Note that the effect of finite blade thickness differs markedly for in-plane and out-of-plane motions. For example, comparing the results for *in-plane* motion of an infinitely thin blade ($A\to\infty$) with that of a thin rectangular cylinder, $A=10$, we find that the hydrodynamic load differs by 41% and 24% in the real and imaginary components, respectively. For *out-of-plane* motion, however, the differences between the infinitely thin case ($A\to 0$) and a thin rectangular cylinder of identical geometry, $A=1/10$, are only 5.0% and 2.1% for the real and imaginary components, respectively.

We remind the reader that in-plane and out-of-plane motions of a thin rectangular cylinder are selected using the aspect ratio in the present formulation—a cylinder of aspect ratio A that undergoes in-plane motion will possess an aspect ratio of $1/A$ for out-of-plane motion. Furthermore, the concept of in-plane and out-of-plane motions is only pertinent in cases where either $A\equiv h/b\gg 1$ or $h/b\ll 1$, since one length scale of the cylinder greatly exceeds the other.

These results demonstrate that the hydrodynamic load induced by a thin rectangular cylinder of finite aspect ratio, $A=1/10$, is well approximated by that of an infinitely thin blade undergoing out-of-plane motion. The agreement improves dramatically as the aspect ratio is reduced further, and we observe an order-of-magnitude improvement in the relative difference with an order-of-magnitude decrease in A.

TABLE II. Percentage relative difference between the hydrodynamic functions for an infinitely thin blade executing in-plane motion and a cylinder of finite aspect ratio. Results are given for $\beta=10$ and $N=10,20,40,80,160$ from which Richardson extrapolation is used.

	Percentage difference	
A	Real	Imaginary
∞	…	…
50	8.6	6.1
20	20	13
10	41	24
5	88	44
2	281	98
1	767	184

TABLE III. Percentage relative difference between the hydrodynamic functions for an infinitely thin blade executing out-of-plane motion and a cylinder of finite aspect ratio. Results given for $\beta=10$ and $N=10,20,40,80,160$ from which Richardson extrapolation is used.

	Percentage difference	
A	Real	Imaginary
0	...	...
1/50	0.87	0.37
1/20	2.4	0.94
1/10	5.0	2.1
1/5	10	5.1
1/2	23	16
1	40	34

Even for thick cylinders, up to an aspect ratio of $A=1/2$, the error induced by approximating the cylinder by an infinitely thin blade is only approximately 20%.

In contrast, in-plane motion does not display the same level of agreement as that exhibited by out-of-plane motion. The percentage relative differences for the same cylinder shape, i.e., $A_{\text{in-plane}}=1/A_{\text{out-of-plane}}$, are approximately an order of magnitude larger than those for out-of-plane motion; see Table II. This indicates that the infinitely thin approximation for in-plane motion should only be used for extremely thin blades, e.g., $A \gtrsim 50$ if accuracy better than 10% is required.

The underlying reason for the difference between the in-plane and out-of-plane results is due to the effects of pressure. For in-plane motion of an infinitely thin blade, the hydrodynamic load is unaffected by the pressure in the fluid, whereas the pressure is the only contributor for out-of-plane motion. Increasing the cylinder thickness from this limiting case then results in a nonzero pressure contribution in the in-plane case at the leading faces of the cylinder. This has a dramatic effect and strongly enhances the overall hydrodynamic load. The results for in-plane and out-of-plane motions demonstrate that (i) the pressure contribution from the leading face dominates (ii) the contribution from the vorticity (shear stress) on the side face in determining the overall hydrodynamic load.

Importantly, the inviscid result ($\beta \to \infty$) establishes that the inertial component of the hydrodynamic load is enhanced for a cylinder of finite thickness executing out-of-plane motion in comparison to the infinitely thin result. Since this load is only dependent on the pressure distribution across the leading face, see Eq. (20), we find that the net pressure jump across the cylinder is enhanced by increasing the cylinder thickness; see Appendix B for a detailed discussion. Results for the viscous case are consistent with this observation, with the added effect of the viscous boundary layer enhancing both the inertial and dissipative components of the load. Comparison of the inviscid and viscous cases for high β shows that enhancement due to the viscous boundary layer and the increase in the inviscid component of the pressure accounts for the marked differences between results for the real and imaginary components in Tables II and III. Namely, for a cylinder of finite thickness the imaginary component displays better agreement with the infinitely thin result than the real component.

C. Practical implications to AFM cantilever calibration

These findings are of great significance in practice, since they provide rigorous justification for the current widespread use of the infinitely thin blade approximation for out-of-plane motion of oscillating beams of finite thickness.[9–15] This is particularly the case for standard experimental techniques, such as the Sader method,[31–35] that use the infinitely thin blade out-of-plane solution as their foundation for quantitative measurement of the stiffness of AFM microcantilevers. Importantly, all practical cantilevers possess a finite aspect ratio (thickness/width). However, the results in Table III establish that there is very little difference in the hydrodynamic load between such practical devices and their infinitely thin counterparts. As such, successful and accurate calibration of AFM microcantilevers using these techniques does not rely on accurate knowledge of the microcantilever thickness.

Importantly, better agreement is observed for the imaginary component than for the real component of the hydrodynamic function, see Table III and discussion above. This is particularly significant, since the Sader method relies only on the imaginary component of the hydrodynamic function—the measured spring constant is directly proportional to the hydrodynamic function [Eq. (4) of Ref. 31],

$$k = 0.1906\rho b^2 L Q \Gamma_i(\omega_R)\omega_R^2, \tag{26}$$

where k is the cantilever normal spring constant, ρ is the fluid density, b the cantilever width, L its length, ω_R the resonant frequency in fluid (air), Q is the quality factor in fluid (air), and Γ_i the imaginary component of the hydrodynamic function for out-of-plane motion of an infinitely thin blade.

We note that intrinsic errors in AFM measurements typically exceed 10%, and are thus larger than many of the entries in Table III. The present findings therefore enable use of (infinitely thin blade) techniques for calibration of thick microcantilever beams, with little compromise in accuracy. For example, Eq. (26) will exhibit an error of only 16% for a relatively thick cantilever beam of aspect ratio (thickness/width) $A=1/2$ (at $\beta=10$).

IV. CONCLUSIONS

We have theoretically investigated the flow generated by oscillating rectangular cylinders of arbitrary aspect ratio (thickness/width) immersed in fluid. Both the general viscous case and the inviscid limit were considered. The underlying principal assumptions were that the oscillation amplitude is small and the flow is incompressible. Both assumptions are satisfied in many cases of practical interest, including devices found in the AFM and NEMS. Since common elastic beam devices found in practice possess aspect ratios that deviate strongly from the infinitely thin limit, the results presented in this study are expected to be of significant practical value.

Importantly, it was found that the infinitely thin blade solution provides an excellent approximation for out-of-plane oscillations of rectangular cylinders of finite aspect ratio (thickness/width): $A<1/2$ ensures accuracy better than approximately 20% in the hydrodynamic load. This provides rigorous justification for use of the infinitely thin blade approximation for out-of-plane oscillations of beams in practice. This is particularly relevant for device characterization techniques found in the AFM and NEMS, where the infinitely thin blade formulation is common place.

The situation changes dramatically for in-plane oscillations, however, where the infinitely thin result is valid only for extremely thin blades: $A>50$ is required for accuracy better than approximately 10%. This result establishes the critical importance of the size of the leading face for in-plane oscillations of thin beams. The difference between the out-of-plane and in-plane results is due to the pressure contribution at the leading face being modified more strongly in the in-plane case relative to the infinitely thin result.

Finally, a database of highly accurate numerical results was presented for a wide range of aspect ratios and normalized frequencies. This is expected to find significant utility in characterization of devices found in AFM and NEMS, and in the benchmarking of future numerical schemes and analytical solutions.

ACKNOWLEDGMENTS

The authors would like to thank Igor Bargatin and Michael Roukes for many interesting discussions relating to NEMS devices. This research was supported by the Australian Research Council Grants Scheme.

APPENDIX A: INFINITELY THIN BLADES

1. In-plane oscillation

We consider an infinitely thin blade oscillating in its own plane, subject to the no-slip boundary condition. To do so, we use the streamfunction presented in Eq. (9) and consider the contour $C_{\text{blade}}=C_+ + C_-$ where C_+ and C_- are the "top" and "bottom" sides of the cut extending from $(-a,0)$ to $(a,0)$ in the (y,z) plane; see Fig. 1(b). Under such conditions, Eq. (9) reduces substantially to become

$$\psi(y',z') = -U_{\text{cyl}}z' + \int_{-a}^{a} 2\bar{\zeta}(y)\Psi_z(y,0;y',z') - \frac{1}{\mu}\Delta\bar{p}(y)\Psi_y(y,0;y',z')dy, \tag{A1}$$

where $\bar{\zeta}=\bar{\zeta}_+=-\bar{\zeta}_-$ is the vorticity distribution across the top face of the blade. By symmetry, the pressure difference $\Delta\bar{p}(y)$ across the blade is equal to zero. Noting this, and setting $z'=0$ after differentiating Eq. (A1) with respect to z', we obtain the following integral equation:

$$2\int_{-a}^{a}\zeta(y)\Psi_{zz'}(y,0;y',0)dy = U_{\text{cyl}}. \tag{A2}$$

We have dropped the "bar" notation for $\zeta(y)$ since the measured vorticity is the same as in the reference frame of the blade. Introducing the dimensionless spatial coordinate $\xi=y/a$, vorticity $\Lambda(\xi)=(a/U_{\text{cyl}})\zeta(y)$, and frequency $\beta=\omega a^2/\nu$, the integral equation becomes

$$2\int_{-1}^{1}\Lambda(\xi)L_{\text{in}}(-i\sqrt{i\beta}|\xi-\xi'|)d\xi = 1, \tag{A3}$$

where the kernel function is defined as

$$L_{\text{in}}(Z) = \frac{1}{2\pi Z} \quad \frac{d}{dZ}[\log Z + K_0(Z)]. \tag{A4}$$

We note that the in-plane motion of the blade is described by the above integral equation involving only the vorticity distribution along the contour. Note also the behavior of the kernel function for small and large values of its argument,

$$L_{\text{in}}(Z) = -\frac{1}{4\pi}\left(\log Z + \gamma - \frac{1}{2} - \log 2\right) + O(Z^2\log Z) \quad \text{for } Z \ll 1, \tag{A5}$$

$$L_{\text{in}}(Z) = \frac{1}{2\pi Z^2} - \frac{1}{\sqrt{8\pi Z}}e^{-Z}\left[\frac{1}{Z} + O\left(\frac{1}{Z^2}\right)\right] \quad \text{for } Z \gg 1. \tag{A6}$$

The integral equation, Eq. (A3), for the vorticity distribution is solved numerically. This involves discretizing the domain $\xi\in[-1,1]$. This integral equation is then transformed into a matrix-vector equation using an appropriate quadrature method and solved. Before implementing this procedure, we note the following features relating to Eq. (A3); these are identical to those discussed by Tuck[24] for the out-of-plane case:

(1) The presence of the logarithmic singularity in the kernel function at $\xi=\xi'$.
(2) The blade under consideration is infinitely thin. At the leading edges, we expect the presence of a square-root singularity.[24] That is, we anticipate square-root singularities in $\Lambda(\xi)$ at $\xi=\pm 1$.
(3) If β is large, then the exponential term in Eq. (A6) oscillates rapidly as it approaches zero.

Given these similarities between the in-plane and out-of-plane cases, we implement an identical numerical scheme to that proposed by Tuck for this in-plane case. Specifically, the interval is discretized using the points $\xi=\xi_j=-\cos(\pi j/N)$, $j=0,\ldots,N$ and we approximate $\Lambda(\xi)$ as a constant on each interval. However, the kernel function L_{in} in the quadrature method is not approximated in each interval. We ensure the equation holds at the midpoint of each interval, $\xi=\xi_k'=\frac{1}{2}(\xi_k+\xi_{k+1})$. Using Eq. (A3) and approximating $\Lambda(\xi)=\Lambda_j=\text{const}$ on each interval $\xi_j<\xi<\xi_{j+1}$ results in the following equation:

$$M_{\text{in}}\mathbf{\Lambda} = \mathbf{1}, \tag{A7}$$

with corresponding matrix elements

$$[M_{\text{in}}]_{kj} = 2\int_{\xi_j}^{\xi_{j+1}} L_{\text{in}}(-i\sqrt{i\beta}|\xi - \xi_k'|)d\xi. \tag{A8}$$

Evaluation of the elements of M_{in} requires numerical computation, and we use the software package MATHEMATICA® for this purpose. After calculation of the vorticity distribution, the hydrodynamic function is evaluated using Eq. (11). Recalling the definitions for the scaled quantities and noting that the dominant length scale is $2a$, we obtain

$$\Gamma(\omega) = \frac{2i}{\pi\beta}\int_{-1}^{1}\Lambda(\xi)d\xi = \frac{2i}{\pi\beta}\sum_{j=0}^{N-1}(\xi_{j+1} - \xi_j)\Lambda_j + O(N^{-2}). \tag{A9}$$

Since the blade is infinitely thin in the z-direction, the fictitious body force contribution [see Eqs. (8) and (11)] resulting from the change in reference frame is zero.

a. High-frequency limit

In the limit of high frequency, in-plane oscillations of an *infinitely thin blade* in the fluid will generate a thin viscous boundary layer near its surface. In this limit, the fluid does not see the width of the blade, thus facilitating the use of an infinite plate solution. Using the well-known solution to Stokes' second problem,[37] we find that the hydrodynamic function can be expressed as

$$\Gamma_\infty(\omega) = \frac{4}{\pi}\sqrt{\frac{i}{\beta}}. \tag{A10}$$

The length scale in Eq. (A10) has been implicitly removed by expressing the hydrodynamic function in terms of the dimensionless frequency β.

2. Out-of-plane oscillation

This problem was originally solved by Tuck,[24] a summary of which is given here. By considering the contour $C_{\text{blade}} = C_+ + C_-$ where C_+ and C_- are the "right" and "left" sides of the cut extending from $(0,-d)$ to $(0,d)$ in the (y,z) plane, the following integral equation is obtained:

$$2\int_{-1}^{1} P(\chi)L_{\text{out}}(-i\sqrt{i\beta}|\chi - \chi'|)d\chi = 1, \tag{A11}$$

where the kernel function is defined as

$$L_{\text{out}}(Z) = \frac{1}{2\pi}\frac{d^2}{dZ^2}[\log(Z) + K_0(Z)], \tag{A12}$$

and the scaled frequency, spatial coordinate, and pressure are given by $\beta = \omega d^2/\nu$, $\chi = z/d$, and $P(\chi) = (d/\mu U_{\text{cyl}})p(z)$, respectively. In a manner completely analogous to the case of in-plane oscillation, the hydrodynamic function is then written in the discretized form

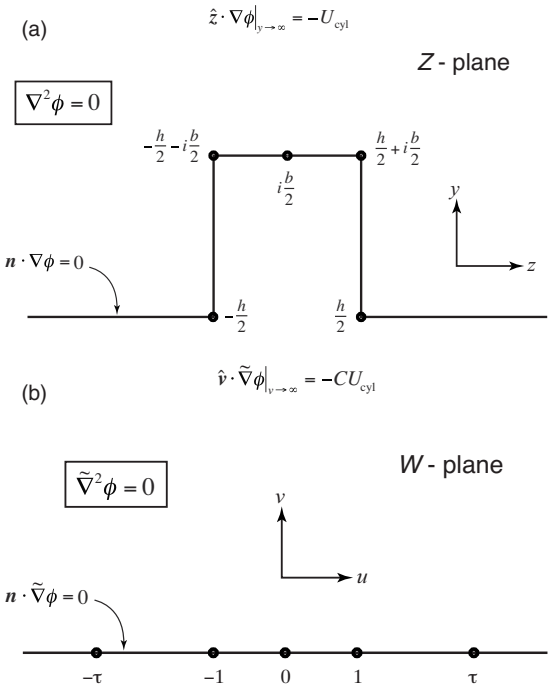

FIG. 11. (a) Schematic diagram showing the upper half of cylinder in the original complex Z-plane. Boundary conditions are as indicated. $Z = z + iy$. (b) Schematic diagram showing the upper half-space of cylinder in the transformed complex W-plane. Transformed Laplacian indicated by the tilde. Transformed boundary conditions as indicated. $W = u + iv$.

$$\Gamma(\omega) = \frac{2i}{\pi\beta}\int_{-1}^{1} P(\chi)d\chi = \frac{2i}{\pi\beta}\sum_{j=0}^{N-1}(\chi_{j+1} - \chi_j)P_j + O(N^{-2}). \tag{A13}$$

The above expression is used to calculate the hydrodynamic function presented in Sec. III A 1.

APPENDIX B: INVISCID FLOW

1. Exact solution

We now consider the case of inviscid flow. This corresponds to the formal asymptotic limit of infinite dimensionless frequency, i.e., $\beta \to \infty$. The flow is again considered to be incompressible throughout and is solved using potential flow theory. The velocity field $\mathbf{u}$ is related to the velocity potential ϕ by

$$\mathbf{u} = \nabla\phi. \tag{B1}$$

The solution to this flow problem is obtained using complex variable analysis. Specifically, conformal mapping of the original cylinder geometry onto a half-space enables the flow field and resulting force to be determined directly. Since the flow is symmetric about the z-axis [see Fig. 1(a)], its solution can be obtained by considering only the region $y \geq 0$; see Figs. 11(a) and 11(b). Note that the calculation is performed in the reference frame of the cylinder as for the viscous case. As such, an additional body force must be included in the final force calculation, as specified in Eq. (8).

The original cylinder geometry in the Z-plane is mapped onto the W-plane using the conformal mapping

$$Z = C\int_0^{W/\tau} \sqrt{\frac{1-\tau^2\zeta^2}{1-\zeta^2}}d\zeta + \frac{bi}{2}, \tag{B2}$$

where

$$C = \frac{b}{2\tau[E(1-m)-mK(1-m)]}, \tag{B3}$$

and K and E are complete elliptic integrals of the first and second kinds, respectively. The parameter $m \equiv 1/\tau^2$ is the root of the transcendental equation

$$\frac{E(m)-(1-m)K(m)}{E(1-m)-mK(1-m)} = \frac{h}{b}. \tag{B4}$$

This mapping is easily derived using the Schwarz–Christoffel transformation[27] with reference to Figs. 11(a) and 11(b). Note that (i) $Z=z+iy$, $W=u+iv$, and (ii) since $\tau>1$, we find that $0<m<1$.

The solution to the Laplace equation for the velocity potential ϕ in the W-plane is simply

$$\phi = -CU_{\text{cyl}}u, \tag{B5}$$

from which the reduced pressure is

$$\bar{p} = -i\rho\omega CU_{\text{cyl}}u. \tag{B6}$$

The total force acting on the cylinder is then obtained by integrating the stress vector. This is easily performed in the complex domain by transforming the resulting integral in the Z-plane into the W-plane. Incorporating the fictitious body force specified in Eq. (8) then yields

$$\mathbf{j}\cdot\mathbf{F} = 4i\rho\omega U_{\text{cyl}}C^2\int_1^{\tau} W\sqrt{\frac{W^2-1}{\tau^2-W^2}}dW - i\rho\omega U_{\text{cyl}}bh, \tag{B7}$$

which reduces to

$$\mathbf{j}\cdot\mathbf{F} = i\rho\omega U_{\text{cyl}}[\pi(\tau^2-1)C^2 - bh]. \tag{B8}$$

Substituting Eq. (B3) into Eq. (B8), and using the definition in Eq. (11), then gives the required exact result for the hydrodynamic function in the inviscid limit

$$\Gamma(\omega) = \frac{b^2}{X^2}\left(\frac{1-m}{[E(1-m)-mK(1-m)]^2} - \frac{4h}{\pi b}\right), \tag{B9}$$

where m is the solution to Eq. (B4) and $X=\max(h,b)=2\kappa$.

2. Asymptotic results

Equation (B9) can be explicitly solved in the asymptotic limits of small and large h/b to yield

$$\Gamma(\omega) \sim 1 - \frac{2h}{\pi b}\left[3+\log\left(\frac{h}{4\pi b}\right)\right] + O\left(\left[\frac{h}{b}\right]^2\right), \quad \frac{h}{b} \ll 1 \tag{B10}$$

and

$$\Gamma(\omega) \sim \frac{2b^2}{\pi^2 h^2}\left[1+2\log\left(\frac{4\pi h}{b}\right)\right] + O\left(\left[\frac{b}{h}\right]^3\right), \quad \frac{h}{b} \gg 1. \tag{B11}$$

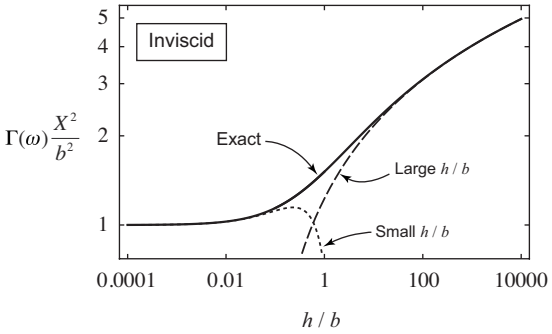

FIG. 12. Comparison of exact and asymptotic results for the normalized hydrodynamic function for inviscid flow as a function of the aspect ratio h/b.

A comparison of these asymptotic results to the exact solution is given in Fig. 12, where good agreement is observed in the limits of small and large h/b. Note that the hydrodynamic function has been normalized so that the width b of the cylinder is the dominant length scale for all aspect ratios A. This differs from the convention used above, but permits direct physical interpretation of the numerical results.[39] Specifically, Fig. 12 illustrates how the true hydrodynamic load varies as the thickness h is increased while the width b is held constant. Interestingly, we observe that the hydrodynamic load rises monotonically as the thickness is increased and asymptotes to a weak logarithmic dependence at large thickness. For example, in the case where the thickness h is 10 000 times larger than the width b, the hydrodynamic load is only a factor of 5 larger than the infinitely thin (zero thickness) case.

The asymptotic analytical results in Eqs. (B10) and (B11) contrast to previous formulas in the literature. Specifically, Yu[30] and Payne[28,29] reported thickness corrections of $O(\sqrt{h/b})$ to the infinitely thin blade result of $\Gamma=1$ when $h/b \ll 1$, rather than the logarithmic correction observed in Eq. (B10). Importantly, these previous theoretical results were obtained either by empirical or heuristic means, and thus have no formal mathematical basis. A similar conclusion is obtained in the opposite limit of $h/b \gg 1$.

[1] A. N. Cleland, *Foundations of Nanomechanics* (Springer-Verlag, Berlin, 2002).
[2] H. G. Craighead, "Nanoelectromechanical systems," Science **290**, 1532 (2000).
[3] Y. T. Yang, C. Callegari, X. L. Feng, K. L. Ekinci, and M. L. Roukes, "Zeptogram-scale nanomechanical mass sensing," Nano Lett. **6**, 583 (2006).
[4] T. P. Burg, M. Godin, S. M. Knudsen, W. Shen, G. Carlson, J. S. Foster, K. Babcock, and S. R. Manalis, "Weighing of biomolecules, single cells and single nanoparticles in fluid," Nature (London) **446**, 1066 (2007).
[5] T. P. Burg, J. E. Sader, and S. R. Manalis, "Nonmonotonic energy dissipation in microfluidic resonators," Phys. Rev. Lett. **102**, 228103 (2009).
[6] S. Boskovic, J. W. M. Chon, P. Mulvaney, and J. E. Sader, "Rheological measurements using microcantilevers," J. Rheol. **46**, 891 (2002).
[7] G. Binnig, C. F. Quate, and Ch. Gerber, "Atomic force microscope," Phys. Rev. Lett. **56**, 930 (1986).
[8] F. J. Giessibl, "Advances in atomic force microscopy," Rev. Mod. Phys. **75**, 949 (2003).

[9]S. Basak, A. Raman, and S. V. Garimella, "Hydrodynamic loading of microcantilevers vibrating in viscous fluids," J. Appl. Phys. **99**, 114906 (2006).
[10]R. J. Clarke, S. M. Cox, P. M. Williams, and O. E. Jensen, "The drag on a microcantilever oscillating near a wall," J. Fluid Mech. **545**, 397 (2005).
[11]C. P. Green and J. E. Sader, "Frequency response of cantilever beams immersed in viscous fluids near a solid surface with applications to the atomic force microscope," J. Appl. Phys. **98**, 114913 (2005).
[12]T. Naik, E. K. Longmire, and S. C. Mantell, "Dynamic response of a cantilever in liquid near a solid wall," Sens. Actuators, A **102**, 240 (2003).
[13]M. R. Paul and M. C. Cross, "Stochastic dynamics of nanoscale mechanical oscillators immersed in a viscous fluid," Phys. Rev. Lett. **92**, 235501 (2004).
[14]J. E. Sader, "Frequency response of cantilever beams immersed in viscous fluids with applications to the atomic force microscope," J. Appl. Phys. **84**, 64 (1998).
[15]C. A. Van Eysden and J. E. Sader, "Frequency response of cantilever beams immersed in viscous fluids with applications to the atomic force microscope: Arbitrary mode order," J. Appl. Phys. **101**, 044908 (2007).
[16]C. A. Van Eysden and J. E. Sader, "Frequency response of cantilever beams immersed in compressible fluids with applications to the atomic force microscope," J. Appl. Phys. **106**, 094904 (2009).
[17]J. W. M. Chon, P. Mulvaney, and J. E. Sader, "Experimental validation of theoretical models for the frequency response of atomic force microscope cantilever beams immersed in fluids," J. Appl. Phys. **87**, 3978 (2000).
[18]C. P. Green and J. E. Sader, "Small amplitude oscillations of a thin beam immersed in a viscous fluid near a solid surface," Phys. Fluids **17**, 073102 (2005).
[19]S. Basak and A. Raman, "Hydrodynamic coupling between micromechanical beams oscillating in viscous fluids," Phys. Fluids **19**, 017105 (2007).
[20]I. Bargatin, E. B. Myers, J. Arlett, B. Gudlewski, and M. L. Roukes, "Sensitive detection of nanomechanical motion using piezoresistive signal downmixing," Appl. Phys. Lett. **86**, 133109 (2005).
[21]I. Bargatin, I. Kozinsky, and M. L. Roukes, "Efficient electrothermal actuation of multiple modes of high-frequency nanoelectromechanical resonators," Appl. Phys. Lett. **90**, 093116 (2007).
[22]I. Kozinsky, H. W. Ch. Postma, I. Bargatin, and M. L. Roukes, "Tuning nonlinearity, dynamic range, and frequency of nanomechanical resonators," Appl. Phys. Lett. **88**, 253101 (2006).
[23]O. Svitelskiy, V. Sauer, N. Liu, K.-M. Cheng, E. Finley, M. R. Freeman, and W. K. Hiebert, "Pressurized fluid damping of nanoelectromechanical systems," Phys. Rev. Lett. **103**, 244501 (2009).
[24]E. O. Tuck, "Calculation of unsteady flows due to small motions of cylinders in a viscous fluid," J. Eng. Math. **3**, 29 (1969).
[25]C. A. Van Eysden and J. E. Sader, "Small amplitude oscillations of a flexible thin blade in a viscous fluid: Exact analytical solution," Phys. Fluids **18**, 123102 (2006).
[26]R. W. Hornbeck, *Numerical Methods* (Prentice-Hall, Englewood Cliffs, NJ, 1975).
[27]R. V. Churchill, *Complex Variables and Applications* (McGraw-Hill, New York, 1960).
[28]P. R. Payne, "The virtual mass of a rectangular flat-plate of finite aspect ratio," Ocean Eng. **8**, 541 (1981).
[29]P. R. Payne, "A unification in the added mass theory of planing," Ocean Eng. **19**, 39 (1992).
[30]Y.-T. Yu, "Virtual masses of rectangular plates and parallelepipeds in water," J. Appl. Phys. **16**, 724 (1945).
[31]J. E. Sader, J. W. M. Chon, and P. Mulvaney, "Calibration of rectangular atomic force microscope cantilevers," Rev. Sci. Instrum. **70**, 3967 (1999).
[32]C. P. Green, H. Lioe, J. P. Cleveland, R. Proksch, P. Mulvaney, and J. E. Sader, "Normal and torsional spring constants of atomic force microscope cantilevers," Rev. Sci. Instrum. **75**, 1988 (2004).
[33]Asylum Research, 6310 Hollister Ave., Santa Barbara, CA 93117, www.asylumresearch.com.
[34]MikroMasch, Akadeemia tee 21, Em 12618 Tallinn, Estonia, www.spmtips.com.
[35]Novascan Technologies, Inc., 131 Main Street, Ames, IA 50010, www.novascan.com.
[36]M. Abramowitz and I. A. Stegun, *Handbook of Mathematical Functions* (Dover, New York, 1972).
[37]G. K. Batchelor, *An Introduction to Fluid Dynamics* (Cambridge University Press, Cambridge, 1974).
[38]A. K. Naik, M. S. Hanay, W. K. Hiebert, X. L. Feng, and M. L. Roukes, "Towards single-molecule nanomechanical mass spectrometry," Nat. Nanotechnol. **4**, 445 (2009).
[39]The length scale convention used in the viscous case is desirable, since it eliminates the singularity and yields a constant value for the hydrodynamic function as $A \to \infty$.